metals

MDPI

Article

Effects of Strength-Modified Grinding on the Surface Microstructure and Mechanical Properties of 30CrMnSiA Bearing Steel

Xiaochu Liu [1,2,3,†], Xiujie Chen [1,2,3,†], Zhongwei Liang [1,2,3,*], Tao Zou [1], Zhaoyang Liu [1,*] and Bin Hu [1,2,3]

[1] School of Mechanical and Electrical Engineering, Guangzhou University, Guangzhou 510006, China
[2] Guangzhou Key Laboratory of Strengthen Grinding and High-Performance Machining, Guangzhou University, Guangzhou 510006, China
[3] Guangdong Research Centre for Strengthen Grinding and High-Performance Micro/Nano Machining, Guangzhou 510006, China
* Correspondence: liangzhongwei@gzhu.edu.cn (Z.L.); liuzy@gzhu.edu.cn (Z.L.)
† These authors contributed equally to this work.

Abstract: The novel strengthen-modified grinding technique (SMGT) treatment was carried out on 30CrMnSiA bearing steels to investigate the effect of jet pressure (0.2–0.6 MPa) and jet angle (30–90°) on its surface micromorphology, microstructure, and mechanical properties. The results show that, under the compound effects of the impact of steel beads and the abrasive powder micro-cutting, the surface of 30CrMnSiA specimens treated by the SMGT has a microstructure with plenty of micropits inside the pits and overlaps between pits. The pit width, depth, and bulge height positively correlate with jet pressure. The pit depth and bulge height positively correlate with jet angle, while the pit width negatively correlates with jet angle. When a pit morphology is produced, plenty of plastic deformation leads to grain refinement, and the lattice distortion induces retained austenite transformation to martensite. Grain refinement and increased martensite content are the main reasons for the significant increase in hardness on the SMGT-treated specimen surface. With the optimized processing parameters, the grain size of the surface was reduced to 10.14 μm, and the martensite content and hardness of the surface layer rose to 51.35% and 377.6 $HV_{0.2}$.

Keywords: 30CrMnSiA steel; strength-modified grinding; micromorphology; microstructure; mechanical property

Citation: Liu, X.; Chen, X.; Liang, Z.; Zou, T.; Liu, Z.; Hu, B. Effects of Strength-Modified Grinding on the Surface Microstructure and Mechanical Properties of 30CrMnSiA Bearing Steel. *Metals* **2022**, *12*, 1713. https://doi.org/10.3390/met12101713

Academic Editor: Umberto Prisco

Received: 26 August 2022
Accepted: 11 October 2022
Published: 13 October 2022

1. Introduction

30CrMnSiA, a high-strength medium carbon steel, has been widely utilized in many industries, such as aero engines and automobiles. Due to its excellent mechanical properties, such as high strength, superior toughness, and hardenability, 30CrMnSiA steel is commonly used in the production of aircraft engine piston materials, crank bearing bushings, aircraft motor frames, and gearbox friction plates [1–6], and has even more excellent prospects for applications. However, the working environment of 30CrMnSiA workpieces is complex and variable. Moreover, for a given application, the 30CrMnSiA material in its original state cannot meet the requirements [7–10], such as high hardness and excellent wear resistance. Appropriate surface treatments must be applied to ensure the quality of 30CrMnSiA workpieces.

Over several decades, plenty of research has been carried out to improve the surface mechanical properties, such as wear resistance and impact resistance, of 30CrMnSiA. Zhou et al. [11] studied the macro- and micro-damage behaviors of 30CrMnSiA steel under the impact of GCr15 steel projectiles. The results showed that, with the decrease in specimen thickness and the increase in projectile velocity, the shape of the specimen surface crater changed to a conical shape, and the specimen on the back side showed an evident

lamellar cracking phenomenon. Fu et al. [12] studied the effects of continuous electron beam treatment on the surface hardening and microstructure changes of 30CrMnSiA investigated experimentally via a multi-purpose electron beam machine pro-beam system. The study found that the microstructure of the electron beam-hardened area is composed of acicular lower bainite, feathered upper bainite, and part lath martensite, and the surface hardness increased 1–3 times with a tiny change of surface roughness. Tang et al. [13] performed a plasma nitrogen carbonitriding treatment of 30CrMnSiA steel with an addition of rare earth. They studied the effects of rare earth on the surface morphology, phase structure, and mechanical properties of the carbonitriding layer. The research found that the nitrocarburized surface hardness showed a decreasing trend, with the rare earth addition increasing in the carrier gas, and the wear resistance of the experimental steel could be improved remarkably by plasma RE nitrocarburizing. Yan et al. [14] used laser quenching technology (LQ) to post-treat ionomer nitriding (PN)-treated 30CrMnSiA steel to improve the surface properties of the specimens and compared the surface microstructure and mechanical properties with those of PN and LQ alone. The results showed that, due to the formation of retained austenite and Fe3O4 in the modified layer of 30CrMnSiA steel after the PN + LQ treatment, the thickness of the modified layer and its hardness and wear resistance were significantly improved compared to the treatment of specimens with PN or LQ alone.

Although the surface hardness of the material treated by the nitriding and laser quenching technique is substantially increased, the modified layer is thin and brittle. Therefore, it cannot withstand excessive contact stresses and impact loads. Since 2008, Liu [15–17] has proposed and engaged in research on the strength-modified grinding technique (SMGT). The SMGT is a new surface treatment technique that integrates surface plasticity strengthening and grinding micro-cutting into one, and the principle is that, under the impetus of compressed gas, the steel beads covered with the strengthened grinding fluids carry the abrasive powder to impact the surface of the workpiece to produce micro-cutting to remove the deterioration layer and significantly improve the surface properties of the workpiece. The introduction of SMGT in metallic materials with improved surface properties has been reported in the past decade [18–21]. The technique can enhance the surface mechanical properties of materials such as roughness, fatigue, corrosion, wear resistance, and impact resistance by forming a thick and strength-modified layer on the surface [22–24]. Therefore, the SMGT is an effective method of surface strengthening and modification and can show perfect universality for many kinds of metallic materials.

In this study, 30CrMnSiA bearing steel was post-treated by the SMGT. The effect of jet pressure and jet angle of the SMGT on the surface micromorphology, microstructure, and microhardness of 30CrMnSiA steel specimens was systematically examined and analyzed. The formation mechanism of the surface microstructure and micromorphology was discussed. The research aims to enhance the surface properties of 30CrMnSiA bearing steel and to provide experimental support for its application in the field of aerospace.

2. Materials and Methods

2.1. Materials

A commercial 30CrMnSiA bearing steel was used as the material in this study. The chemical composition of the 30CrMnSiA bearing steel was tested by an energy dispersive spectrometer (EDS, Oxford X-Max 50, Oxford, UK) and is shown in Table 1. The heat treatment process is as follows: the material is placed in the heating furnace at an austenitizing temperature of 880 °C for 45 min, removed, and quickly put into diesel oil for oil cooling and quenching, then put into the holding furnace at a tempering temperature of 540 °C for 180 min, and finally removed and air-cooled to room temperature of 25 °C. The heat-treated 30CrMnSiA bearing steel was ground and polished by 180–1500 # sandpaper to ensure the surface roughness R_a is below 1.6 μm. Several samples with a dimension of 30 mm × 15 mm × 10 mm were cut from the polished 30CrMnSiA bearing steel using

electrical discharge machining (EDM) wire cutting. Before the SMGT treatment, samples were ultrasonically cleaned in a solution of alcohol and dried.

Table 1. Chemical composition of 30CrMnSiA Steel (wt. %).

Material	Cr	C	Mn	Si	S	P	Fe
30CrMnSiA	0.96	0.37	0.94	1.06	≤0.01	≤0.01	Bal.

2.2. Strength-Modified Grinding and Preparation Scheme

Figure 1 shows the schematic illustration of the treatment process on the SMGT and the setting of the parameters. During the procedure, a three-phase mixed jet comprises the steel beads, the abrasive powder, and strengthened grinding fluids. Steel beads with a particle size of 0.8 mm were selected. Alumina powder with a particle size of 1.3 μm and an average Vickers hardness of 2.2×10^5 MPa was used as the abrasive powder. The strengthened grinding fluids consisted of concentrated modified solutions and distilled water [25,26].

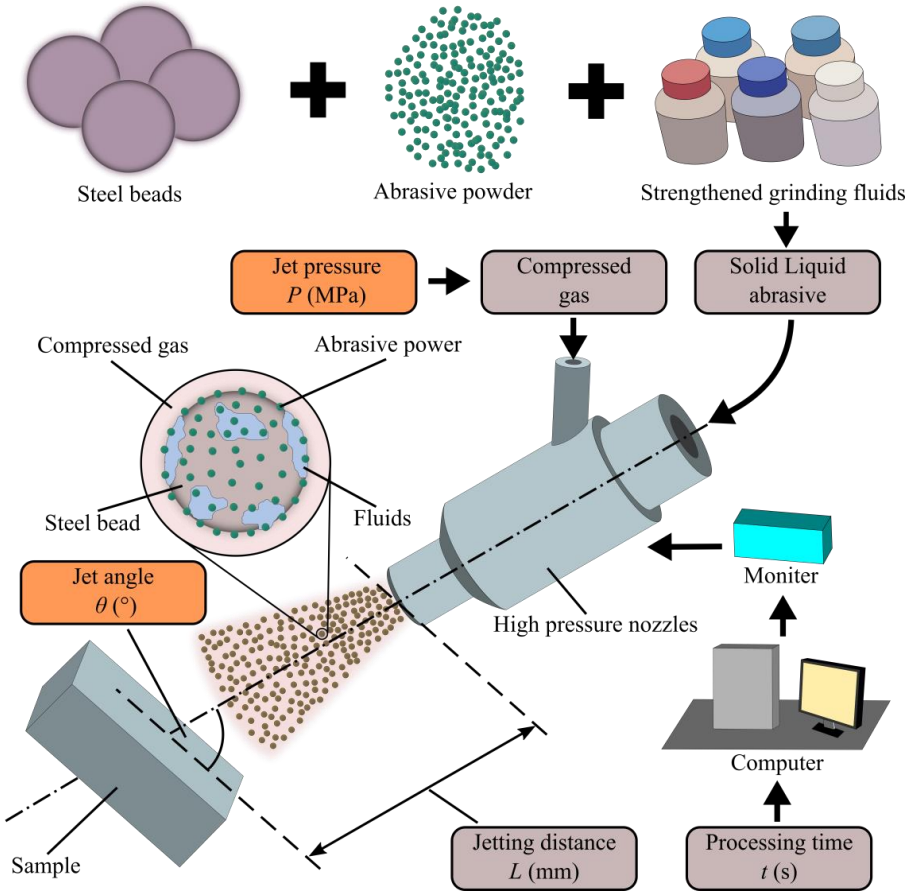

Figure 1. Parameter setting and schematic illustration of the treatment process in SMGT.

The concentrated modified solution is prepared with borax, triethanolamine, and benzotriazole in a particular ratio, and the specific composition content is shown in Table 2.

A single-factor design method was used to investigate the effects of the jet pressure and jet angle of the SMGT on the micromorphology, microstructure, and mechanical properties of the surface layer on the specimens. The processing scheme for the experimental groups is shown in Table 3. A homemade strength-modified grinding processing equipment treated the surface of the samples, which was then ultrasonically cleaned with 95% alcohol and acetone, then dried to obtain the SMGT samples.

Table 2. Composition ratio of the strengthened grinding fluids.

Composition	Chemical Formula	Weight (%)
Borax	$Na_2B_4O_7{\cdot}10H_2O$	25
Triethanolamine	$C_6H_{15}NO_3$	10
Benzotriazole	$C_6H_5N_3$	13
Distilled water	H_2O	50
Others	None	2

Table 3. Parameters of single-factor test.

Group	Jet Pressure (MPa)	Jet Angle (°)	Jetting Distance (mm)	Process Time (s)
T0	none	none	none	none
T1	0.2	90		
T2	0.4	90		
T3	0.6	90	90	900
T4	0.6	60		
T5	0.6	30		

2.3. Characterization

After the strength-modified grinding process treatment to obtain SMGP samples, the micromorphology of the specimen surface layer was observed and analyzed under a scanning electron microscope (SEM, TESCAN MIRA4, TESCAN Inc., Brno, Kohoutovice, Czech Republic) and the white light interferometer (Rtec UP-3000, Rtec instruments Inc., Silicon Valley, CA, USA).

To identify the phase compositions of the specimens treated by SMGT, X-ray diffraction (XRD) analysis was carried out on the surface. A X-ray diffractometer (XRD, Rigaku Smartlab9, Rigaku Corp, Akishima, Japan) was applied in this study. The SMGT samples were tested by Cu-Kα radiation (λ = 0.1542 nm) in the glancing angle range of 30°–90° and recorded with a 1° interval step at 40 kV and 30 mA. The metallographic samples were cut from the cross-sections of the SMGT samples. They were polished and etched with the picric acid solution (picric acid 4 g, hydrochloride 1 mL, ethanol 96 mL, and dodecylbenzene sulfonate 5 g). An metallographic microscope (Mshot MJ42, Mshot Co., Guangzhou, China) observed the SMGT metallographic samples, and the grain size of the processed surface was calculated in conjunction with image-pro plus (IPP) software. Based on the Williamson–Hall method [27], the lattice deformation and the dislocation density of the surface layer were calculated as follows:

$$\varepsilon = \frac{\Delta d}{d} = \left(\beta_{\mathrm{hkl}}\frac{cos\theta}{\lambda} - \frac{0.9}{D_{\mathrm{hkl}}}\right)\frac{\lambda}{2sin\theta}, \quad (1)$$

$$\rho = 14.4\frac{\varepsilon^2}{b^2}. \quad (2)$$

where ε is the lattice deformation, β_{hkl} is the full width at half maximum (FWHM) of the diffraction peak, k is the diffraction factor, D_{hkl} is the average grain size, θ is the diffraction angle, and b is the Burgers vector (b = 0.248 nm). The cross-section microstructures were etched using an alcohol solution containing 4% (vol. %) nitric acid. SEM observed the microstructure of the SMGT metallographic specimens. Furthermore, the martensite content can be calculated by Image-Pro Plus software (IPP, Image-Pro Plus 6.0, Media Cybernetics Inc., Bethesda, Maryland, MD, USA).

The hardness profiles of cross-sections were measured with an microhardness tester (HV-1000, Shanghai Wanheng Precision Instruments Co. LTD, Shanghai, China). The diamond indenter was used for the hardness test, the test load was set at 200 g, and the load time was kept at 10 s. Five indentations placed at the same depth into the cross-section were used to prepare the hardness profiles. Moreover, the effective hardened layer depth is

defined as the distance from the surface to the position where the hardness corresponds to the matrix hardness plus 20 $HV_{0.2}$.

3. Results

3.1. Surface Micromorphology Analysis

The SEM image of the surface layer of the sample is shown in Figure 2. In the image, the size of the white wireframe is 400 μm × 300 μm, and the size of the yellow wireframe is 10 μm × 8 μm. The sample surface of the control group T0 is shown in Figure 2a, and it is not difficult to notice that there are 3–5 interlaced scratches distributed in the white wireframe area, and the surface is relatively smooth and flat.

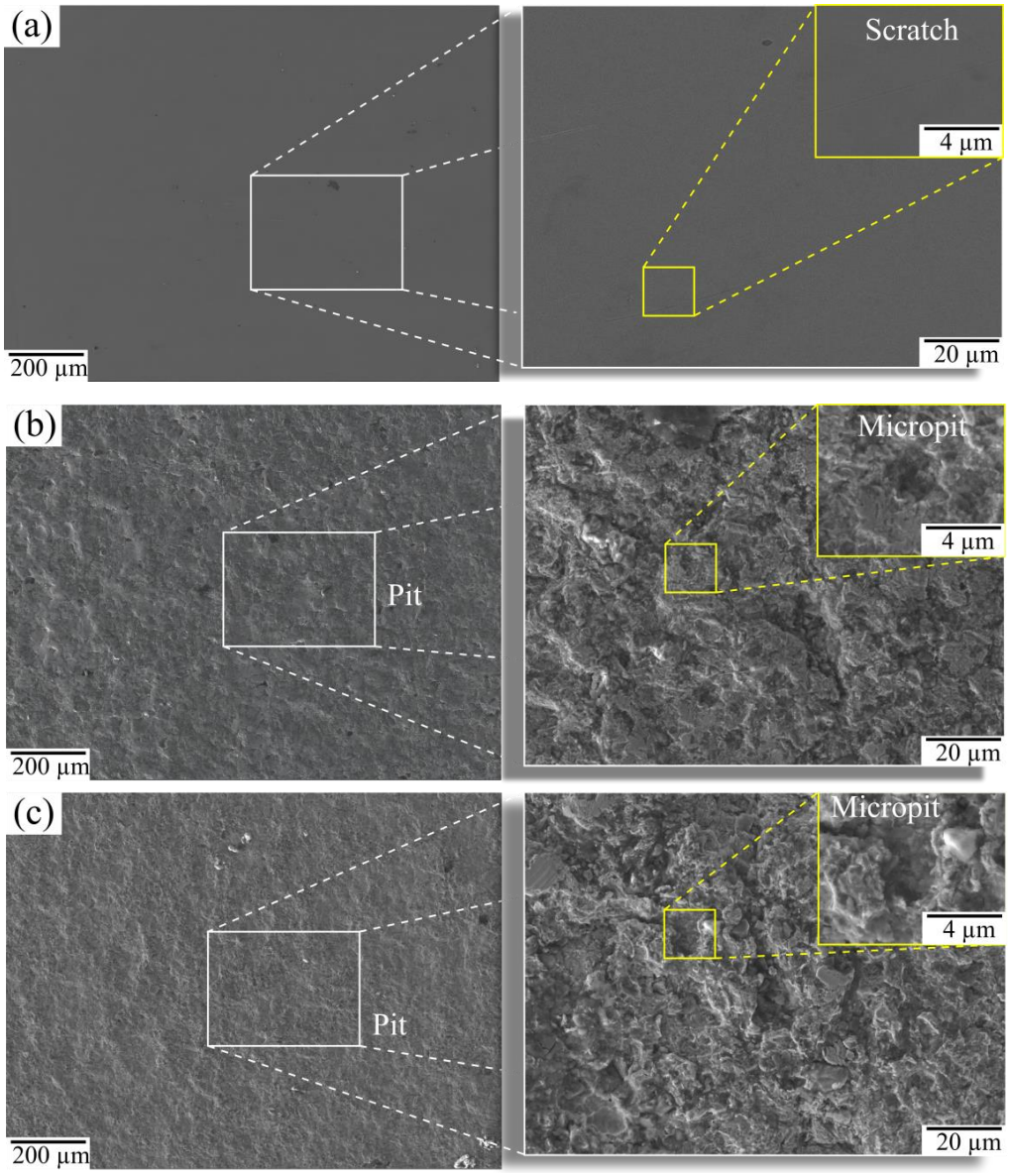

Figure 2. *Cont.*

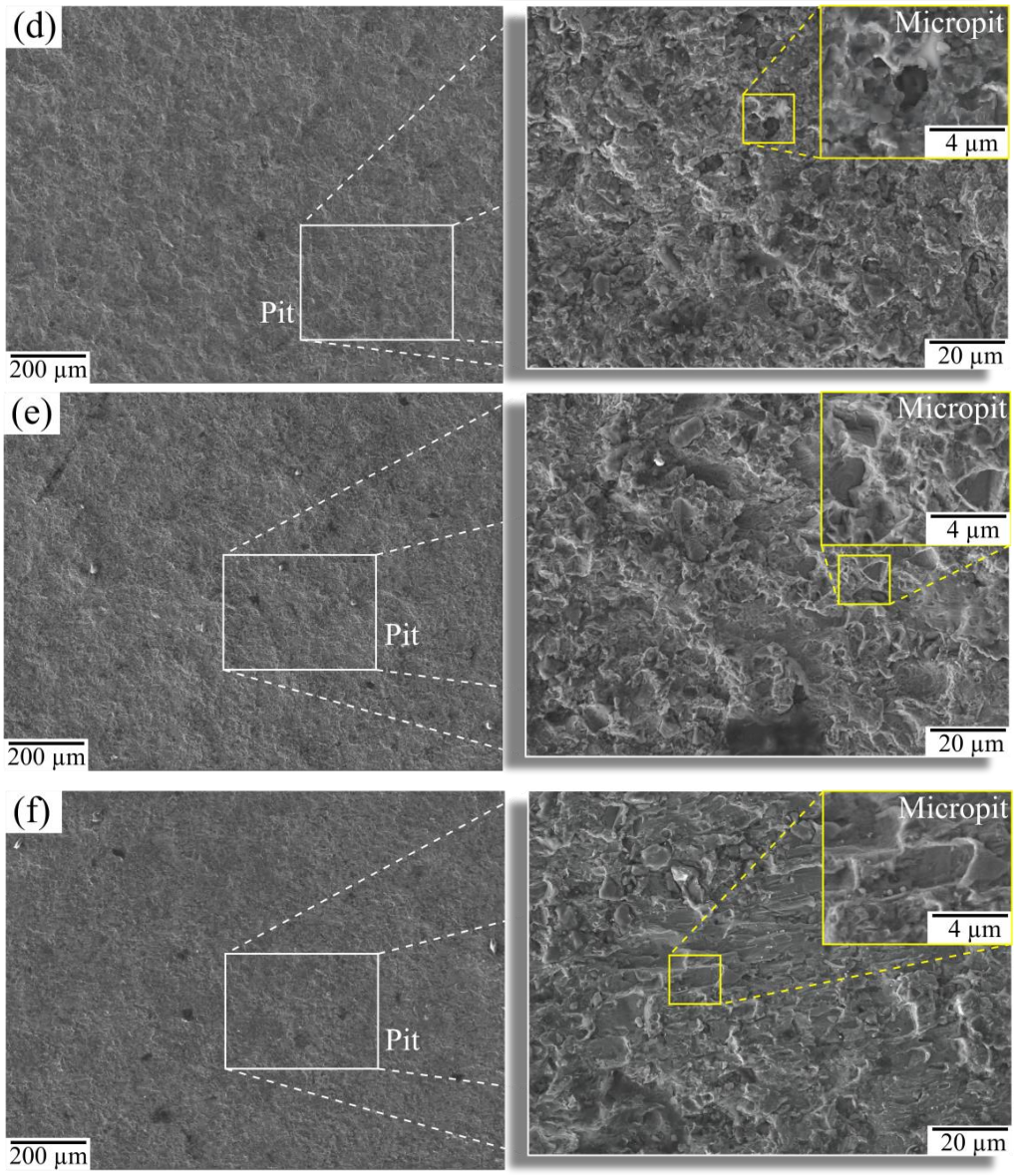

Figure 2. SEM micrograph of surface microstructure of samples. (**a**) control group T0; (**b**) group T1; (**c**) group T2; (**d**) group T3; (**e**) group T4; (**f**) group T5.

In contrast, as shown in Figure 2b–f, the morphology of the processed surface of samples treated with the SMGT shows plenty of disordered and confused micropits. The diameters of the surface micropits in groups T1–T3 were all in the range of 1 μm–4 μm. When the jet pressure of the SMGT is 0.2 MPa, 40–50 micropits were distributed in the white wireframe area on the processed surface of group T1. When the jet pressure increases to 0.4 MPa, micropits on the processed surface of group T2 become denser, and the number of micropits in the white wireframe area rises to 65–80. When the jet pressure attains 0.6 MPa, the density of the micropits further increases, and the number of micropits in the white wireframe area on the processed surface of group T3 is seen to reach 100–120. The density of micropits in the white wireframe area of groups T5, T4, and T3 are similar. At the jet angle of 30°, the micropit on the processed surface of group T5 shows a strip with a size of about 4 μm × 3 μm. When the jet angle was increased from 30° to 60°, the processed surface of group T4 showed a morphology of micropits with a diameter of about 3 μm. When the jet angle was increased to 90°, the diameter of the micropits decreased to about 2 μm. In conclusion, the number of micropits created by the SMGT on the processed surface cause the smoothness of the processed surface to deteriorate. Furthermore, the smoothness of

the processed surface decreases with the rising jet pressure and reduces with the rising jet angle. The surface of 30CrMnSiA bearing steel samples is rough after the SMGT treatment.

To further investigate the pit morphology of the processed surface, the surface profile of the samples was characterized by a white light interferometer, and the size of the photographic area was 1.5 mm × 1.2 mm, as shown in Figures 3 and 4. The processed surface of the T0 control group sample, shown in Figure 3a, is distributed with 20–30 bulges, and 80% of the bulges are distributed on the sides of the scratches, and the average surface height fluctuates between −0.47 μm and 0.5 μm in its direction along the X-axis. In contrast, the surface morphology of the samples in groups T1–T5 is disorganized, and the microstructure has plenty of micropits inside the pit and overlapping pit to pit, as shown in Figure 3b–f. The number of pits appearing on the processed surface of groups T1–T5 ranged from 50 to 70, and the bulge was distributed in the extrusion area between the pits. The fluctuations of the average surface height in the X-axis direction for groups T1 to T5 were −1.08 μm–1.22 μm, −1.47 μm–1.82 μm, −2.14 μm–1.85 μm, −1.73 μm–1.41 μm, and −1.68 μm–1.34 μm, respectively.

Combined with Figures 3b–d and 4, it can be seen that the pits with a width and depth of 123 μm and 1.57 μm, respectively, are distributed on the surface layer of group T1 under 0.2 MPa jet pressure. There are bulges with an average height of 0.62 μm between two adjacent pits. The pit width and depth on the processed surface of group T2 under 0.4 MPa jet pressure are 166 μm and 2.64 μm, respectively, and the bulge height is 1.41 μm. For the processed surface of group T3 with a 0.6 Mpa jet pressure, the pit width increased to 221 μm, the depth increased to 3.52 μm, and the bulge height rose to 1.73 μm. Compared with group T1, the pit width was increased by 34.96% and 79.67%, respectively, the pit depth was increased by 68.15% and 124.20%, respectively, and the bulge height was increased by 127.42% and 179.03% in groups T2 and T3, respectively. Meanwhile, it can be seen from Figures 3d–f and 4 that the processed surface of group T5 with a 30° jet angle, the pit width and depth are 273 μm and 1.18 μm, respectively, and the bulge height is 0.48 μm. The pit width on the surface layer of the group T4 sample at a 60° jet angle was reduced to 248 μm, while the pit depth increased to 1.71 μm and the bulge height reached 0.64 μm. The pit width on the processed surface of group T3 at a 90° jet angle was decreased to 221 μm, while the pit depth and the bulge height increased sharply to 3.52 μm and 1.73 μm, respectively. Compared with group T5, the pit width on the surface layer of groups T4 and T3 decreased by 9.16% and 19.05%, and the pit depth increased by 44.92% and 198.31%, respectively, and the bulge height increased by 33.33% and 260.42%, respectively.

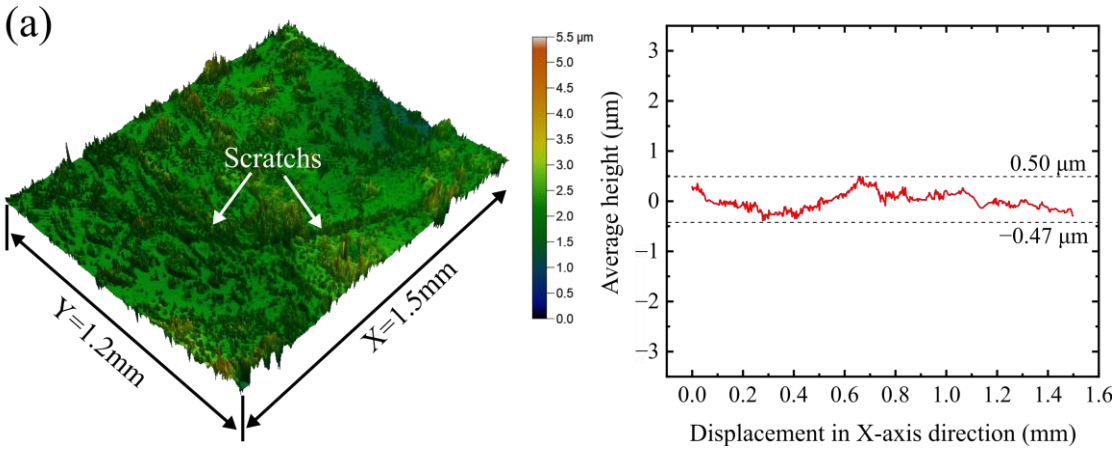

Figure 3. *Cont.*

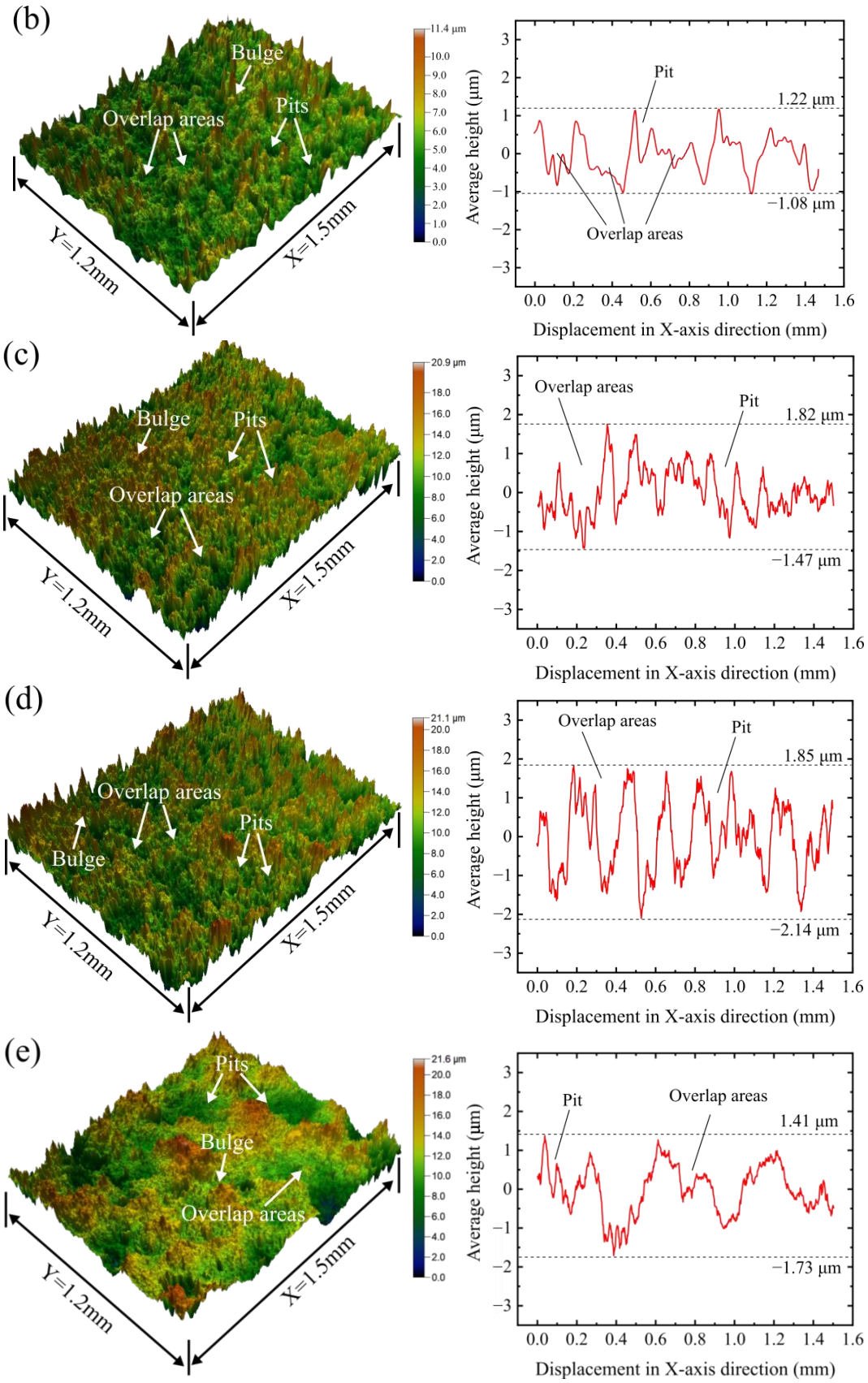

Figure 3. *Cont*.

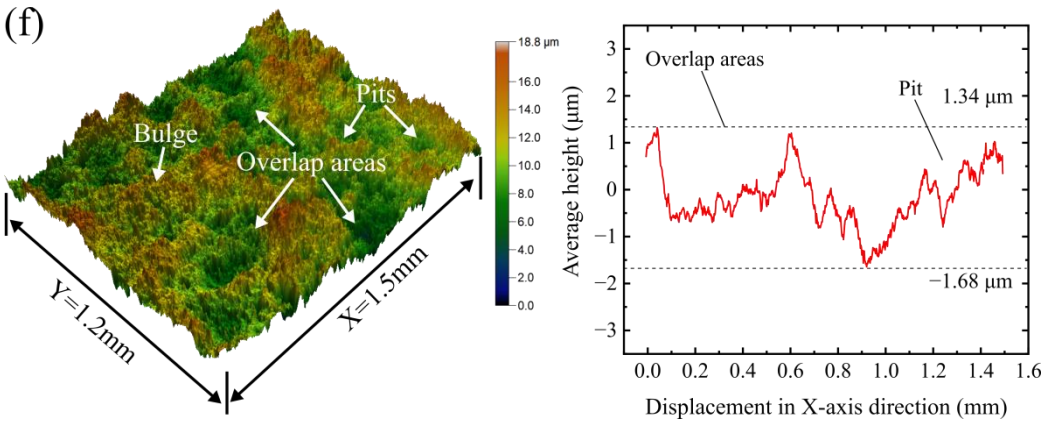

Figure 3. Three-dimensional morphology and two-dimensional profile of specimens: (**a**) control group T0; (**b**) group T1; (**c**) group T2; (**d**) group T3; (**e**) group T4; (**f**) group T5.

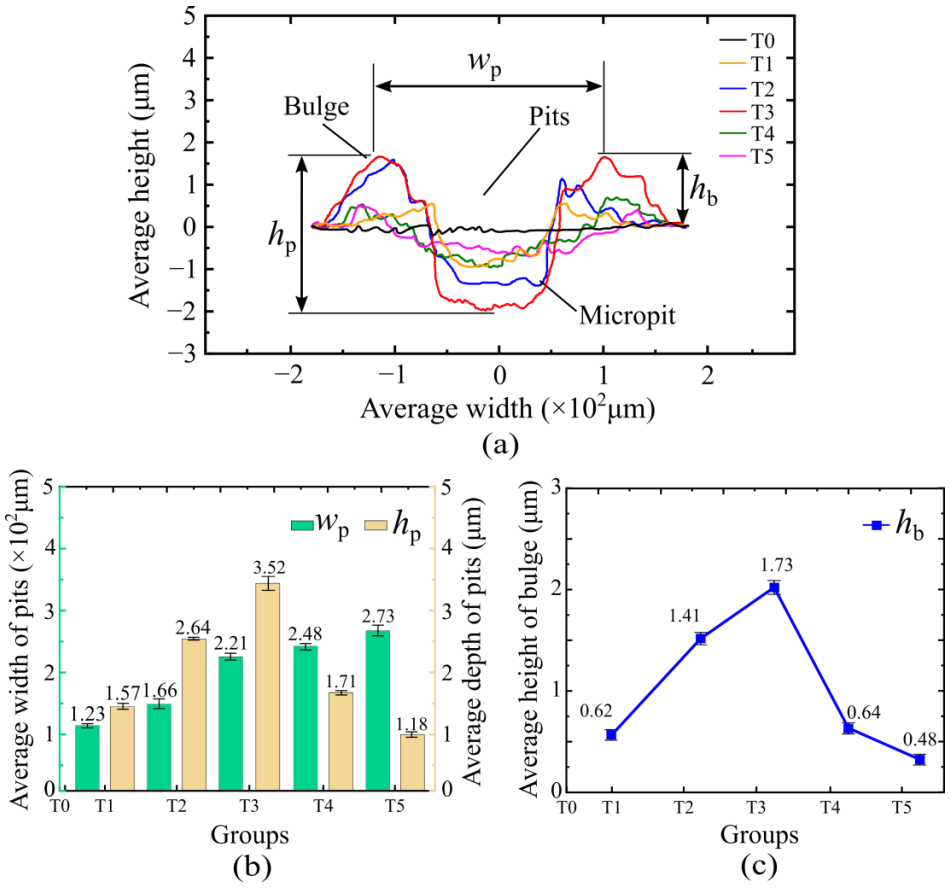

Figure 4. (**a**) Two-dimensional profile of pits of specimens; (**b**) Width and depth of pits of specimens; (**c**) Height of bulge around pits of specimens.

3.2. XRD and Surface Microstructure and Analysis

Figure 5 shows the XRD patterns in the surface layer microstructure of groups T0–T5. In the diffraction angle range of 30° to 90°, there is a diffraction peak of martensite (110), martensite (211), and retained austenite (200). No diffraction peaks of carbide are seen due to the low content and diffuse distribution. The diffraction intensity of retained austenite (200) in the sample surface of control group T0 is the highest, at 557 a.u., and the diffraction intensity of retained austenite (200) in the surface of groups T1–T5, which had been treated by the SMGT, were lower than control group T0, at 385 a.u., 307 a.u., 222 a.u., 332 a.u., and 407 a.u., respectively. The diffraction intensity of martensite (110) in the processed surface

of groups T1–T5 was increased compared with group T0, with the most considerable diffraction intensity of 5656 a.u. in group T3. In addition, it can be seen that the diffraction peak of martensite (110) in the surface layer of control group T0 has the smallest FWHM of 0.2312. The diffraction peak of martensite (110) in the processed surface of groups T1–T5 is broadened, which rose by 0.0170, 0.0392, 0.0508, 0.0309, and 0.0094, respectively, compared with control group T0.

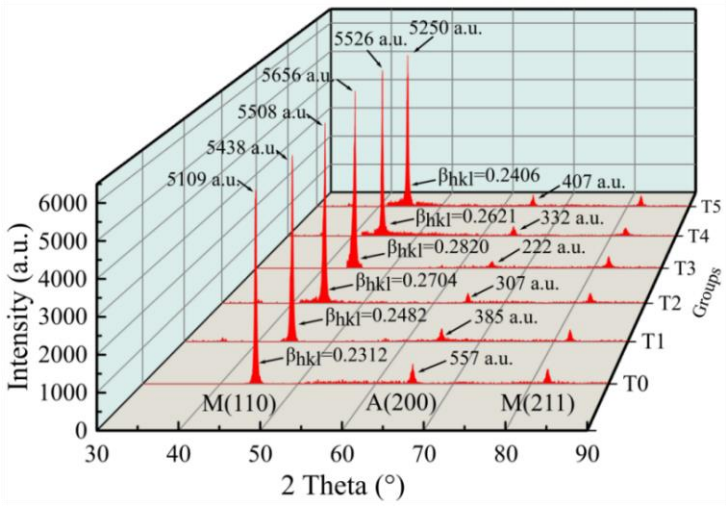

Figure 5. X-ray diffraction pattern on the specimen surface layer of groups T0–T5.

The grain size etching results of the samples are shown in Figure 6. It is not difficult to notice that the grain size of the control group T0 was the largest and distributed equally, while that of the group T1-T5 samples treated by the SMGT was reduced compared to that of the control group. With the jet angle of the SMGT rising from 0.2 MPa to 0.6 MPa, the uniformity degree of the grain size on the processed surface of the tested samples is reduced. Meanwhile, the uniformity degree of the grain size is also reduced as the jet angle rises from 30° to 90°. This indicates that, compared with the control group T0, the grain size of the surface layer on the samples treated with the SMGT was refined.

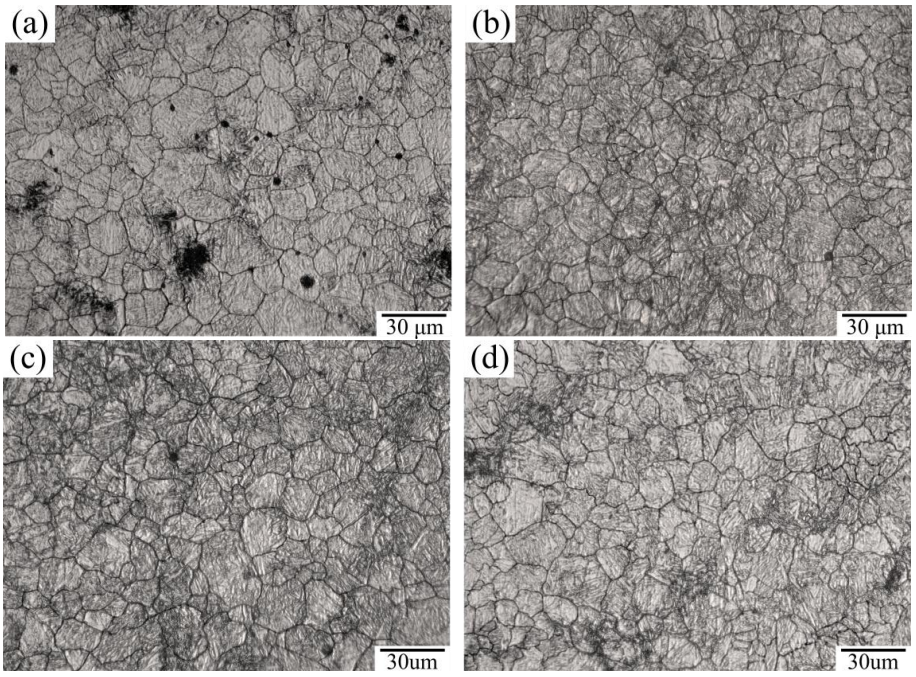

Figure 6. *Cont.*

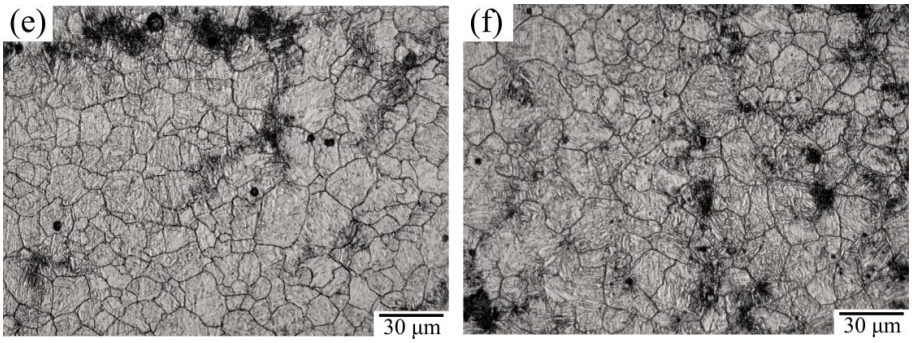

Figure 6. Grain size etching diagram. (**a**) Control group T0; (**b**) group T1; (**c**) group T2; (**d**) group T3; (**e**) group T4; (**f**) group T5.

To further evidence the conclusion, the grain size and lattice distortion of the surface layer of the samples were calculated by IPP software and Formula (1), respectively, and the results are shown in Figure 7a. The average grain size in the surface layer of control group T0 is 17.40 μm, while the grain size in the surface microstructure of groups T1–T5 with the SMGT treatment is 14.11 μm, 12.62 μm, 10.14 μm, 13.35 μm, and 15.60 μm, respectively, and the grain size of group T3 is smallest, at 10.14 μm. In addition, the lattice distortion in the surface layer of control group T0 was the smallest at 0.27, and the lattice distortion in the processed surface layer of groups T1 to T5 was more significant than that of the control group, at 0.29, 0.32, 0.33, 0.31, and 0.28, respectively. Compared to the control group, the lattice distortion in the processed surface layer of groups T1–T5 increased by 6.517%, 15.98%, 19.81%, 21.83%, and 3.57%. From Figure 7b, the average grain size in the diffraction direction decreases from 14.11 μm to 10.14 μm as the jet pressure rises from 0.2 MPa to 0.6 MPa, and from Figure 7c, in the range of 30°–90°, the average grain size also decreases with the increase in the jet angle, from 15.61 μm to 10.14 μm.

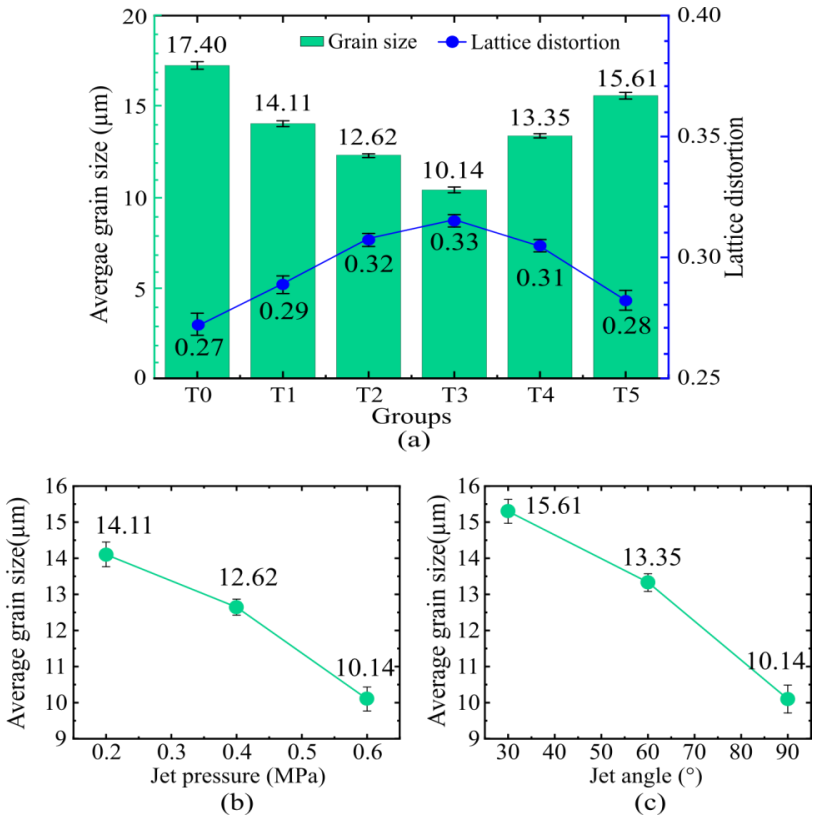

Figure 7. (**a**) The average grain size and lattice distortion of specimens; (**b**) Variation of average grain size with jet pressure; (**c**) Variation of average grain size with jet angle.

The dislocation density results in the surface layer of groups T0–T5 are shown in Figure 8. The dislocation density of control group T0 was 16.91 nm^{-2}. It can be seen that the dislocation density of groups T1–T5 increased compared with control group T0, which were 19.19 nm^{-2}, 22.75 nm^{-2}, 24.23 nm^{-2}, 21.40 nm^{-2}, and 18.14 nm^{-2}, respectively. Dislocation is a physical property of the material and plays a vital role in plasticity, hardness, and wear resistance [28,29]. When the dislocation density of the material is more significant, dislocations accumulate more around the grain or matrix structure to form the tangled and stacked dislocation, dramatically raising the deformation resistance of the grain and microstructure, thus becoming more stable and having a strengthening effect. It can be preliminarily shown that the surface layer of the 30CrMnSiA specimen was strengthened by the SMGT treatment.

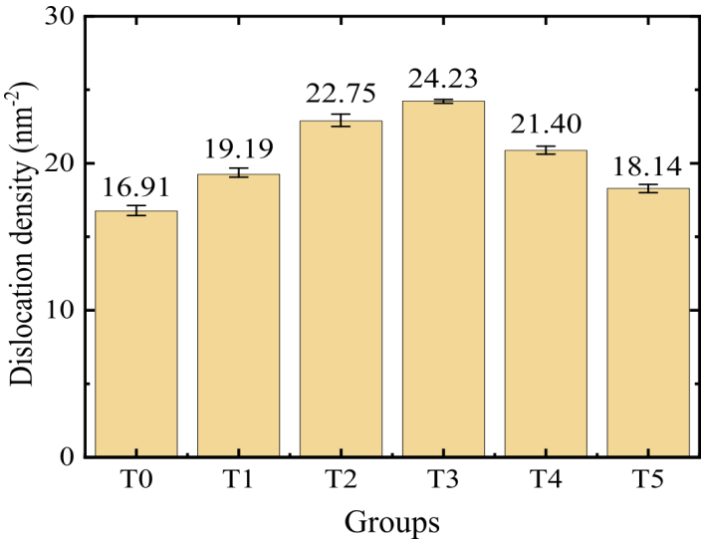

Figure 8. Dislocation density in the surface microstructure of specimens.

The SEM image of the sample surface with the control group and the SMGT treatment is shown in Figure 9. The main components of 30CrMnSiA bearing steel are martensite (M), retained austenite (A), and carbide particles. As shown in Figure 9a, the martensite in the surface layer of control group T0 shows short needles. In contrast, the long-needle martensite and martensite beams (marked by white dashed circles) appear in the processed surface layer of groups T1–T5 with the SMGT in Figure 9b–f. Martensite beams are formed by overlapping martensites that are parallel or intersect at certain angles, with twin crystalline relationships between adjacent martensite sheets [30–32], which show as dark after corrosion due to there being plenty of crystalline interfaces and overlap.

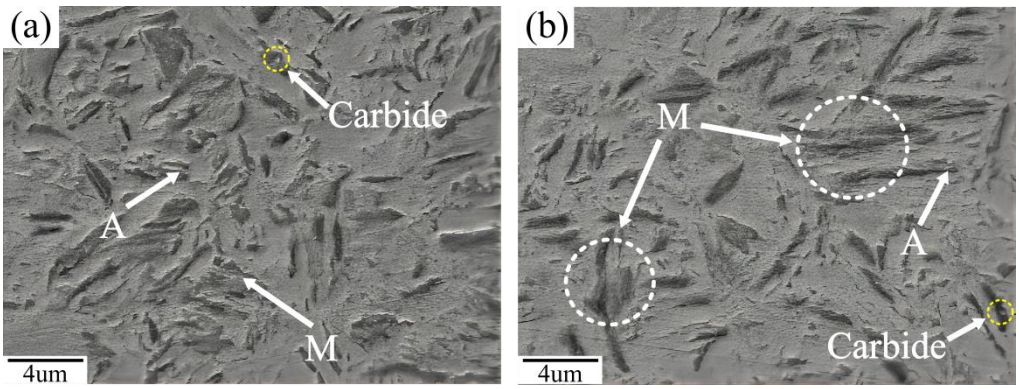

Figure 9. *Cont.*

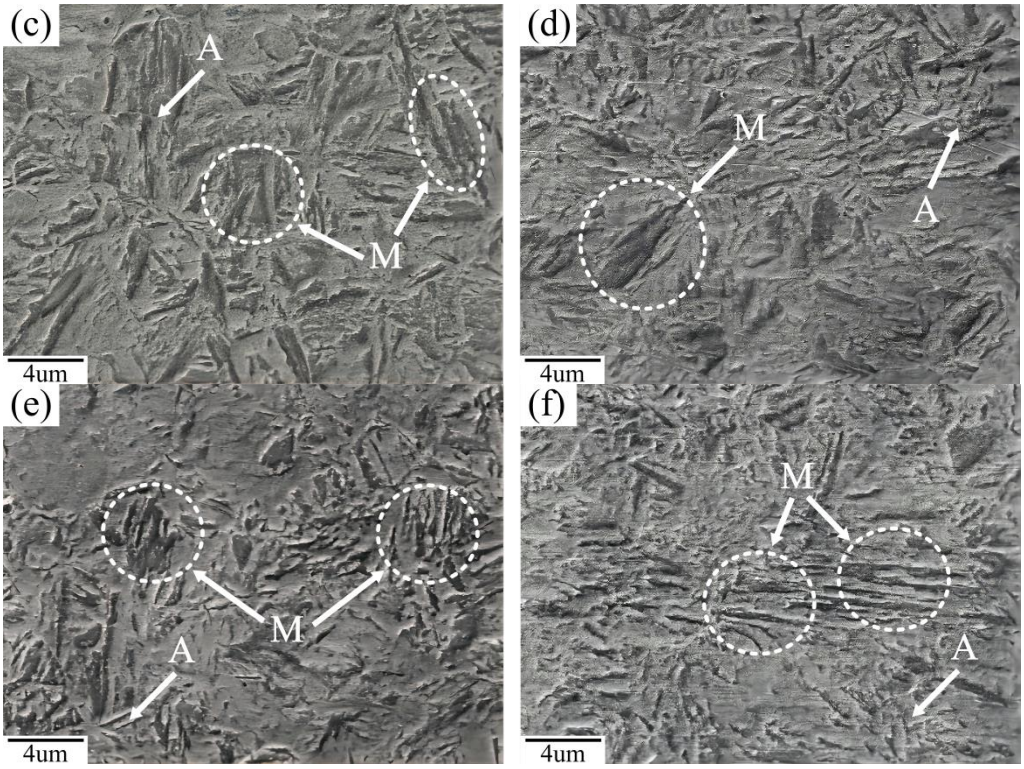

Figure 9. SEM image of processed surface. (**a**) control group T0; (**b**) group T1; (**c**) group T2; (**d**) group T3; (**e**) group T4; (**f**) group T5.

The martensite content in the surface layer of the sample is shown in Figure 10a. It can be seen that the martensite content in the surface layer of control group T0 is the smallest, at 44.16%. Compared with control group T0, the martensite content in the processed surface of groups T1–T5 increased to 45.93%, 47.62%, 51.35%, 49.04%, and 46.27%, respectively. Figure 10b–c shows that the martensite content in the processed surface is positively correlated with the jet pressure and jet angle. The jet pressure went from 0.2 MPa to 0.6 MPa, the content rose from 45.93% to 51.35%, and the content growth rate increased from 8.45%/MPa to 18.65%/MPa. With a jet angle from 30° to 90°, the martensite content increased from 46.27% to 51.35%, and the content growth rate decreased from 0.092%/° to 0.077%/°.

3.3. Section Microhardness Analysis

There was an essential correlation between the wear resistance of the metal material and its surface hardness [33,34]. It can be seen in Figure 11 that the hardness of control group T0 was 310 $HV_{0.2}$. The surface hardness of groups T1–T5 was higher than that of group T0, which was 344.2 $HV_{0.2}$, 356.8 $HV_{0.2}$, 377.6 $HV_{0.2}$, 362.4 $HV_{0.2}$, and 350.1 $HV_{0.2}$, respectively, and its cross-sectional hardness tends to fluctuate and decrease in the depth direction, eventually remaining uniform in the hardness of matrix material. The T3 group showed the most significant increase in the near-surface hardness value of 67.6 $HV_{0.2}$ (an increase of around 21.81%), reaching a hardness of 377.6 $HV_{0.2}$ on the surface, which fluctuated from 377.6 $HV_{0.2}$ to around 310 $HV_{0.2}$ as the depth from the surface layer from 0 um increased to 954 um.

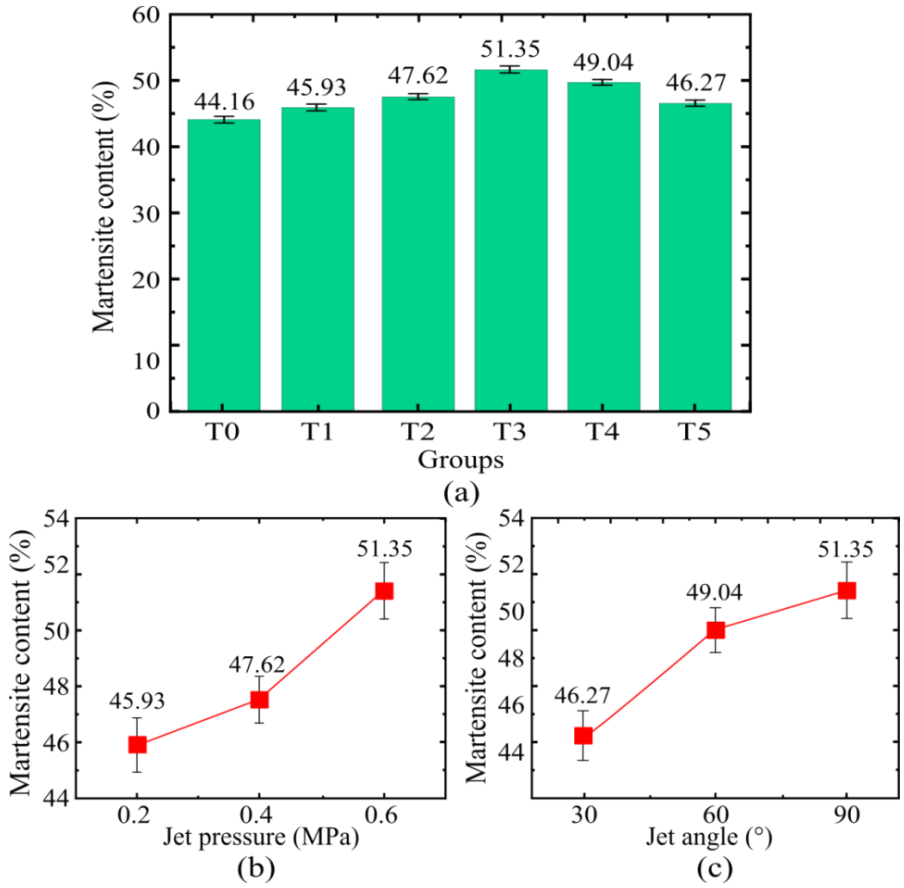

Figure 10. (**a**) Martensite and retained austenite content of processed surface; (**b**) Martensite content changes with jet pressure; (**c**) Martensite content changes with jet angle.

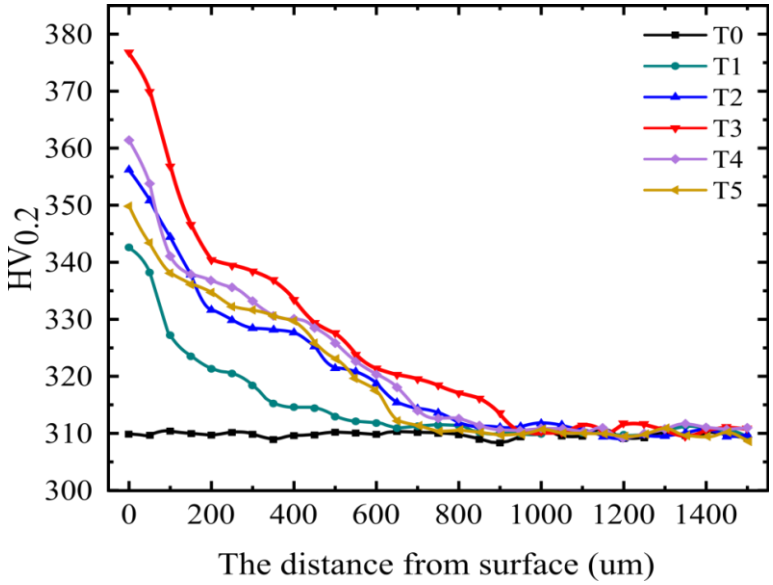

Figure 11. Microhardness profiles in cross-sections of samples.

The hardness of the specimen surface increased from 344.2 $HV_{0.2}$ to 377.6 $HV_{0.2}$ as the jet pressure increased from 0.2 MPa to 0.6 MPa. The surface hardness of group T2 is higher than that of group T1 at 12.6 $HV_{0.2}$, and group T3 is higher than that of group T2 at 20.8 $HV_{0.2}$. Comparing the surface hardness of groups T3–T5, it can be seen that with a jet

angle from 30° to 90°, group T4 has a surface hardness that is 12.3 $HV_{0.2}$ higher than that of group T5, and the T3 group is higher than that of group T4 by 15.2 $HV_{0.2}$.

4. Discussion

In this study, the energy conversion during the SMGT treatment can be divided into two stages. Incidence stage: The initial impact kinetic energy of the three-phase mixed abrasive is converted into deformation energy of the processed surface microstructures. Rebound stage: The elastic deformation of the processed surface microstructures returns part of the kinetic energy to the abrasive. Most of the kinetic energy is transformed into the plastic deformation energy of the processed surface due to plasticity contact. As shown in Figure 12, a steel bead with n abrasive powder attached to its surface is propelled by compressed air with pressure P, jets out from a nozzle pipe of length S, shoots onto the process surface with velocity v_1 and angle α, then bounces back with a velocity v_2 and angle α'.

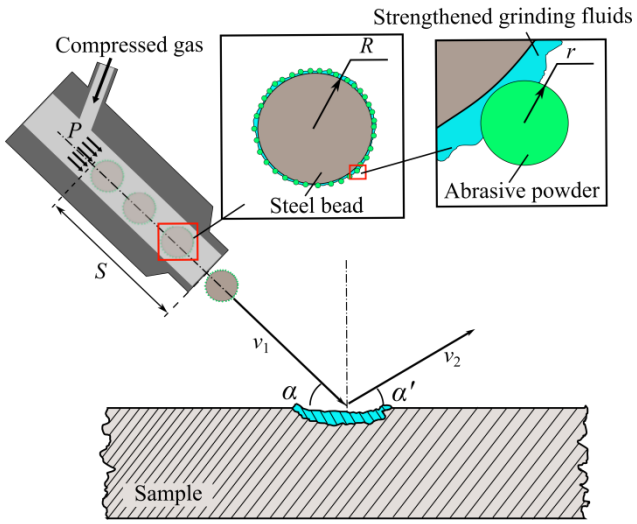

Figure 12. Schematic view of impact principle.

The initial total kinetic energy E_{Total} and initial velocity v_1 before the impact can be obtained, respectively, by:

$$E_{\text{Total}} = \frac{1}{2}(M + nm){v_1}^2 = FS = P\pi(R + r)^2 S \tag{3}$$

$$v_1 = (R + r)\sqrt{\frac{2P\pi S}{M + nm}} \tag{4}$$

where M and m are the masses of the steel beads and the abrasive powder, respectively; R and r are the radius of the steel beads and abrasive powder, respectively. Regarding steel beads and abrasive powders as rigid, the energy conversion rate and plastic deformation energy in the surface layer can be obtained, respectively [35], by:

$$K = 1 - \left(\frac{v_2 sin\alpha'}{v_1 sin\alpha}\right)^2 \tag{5}$$

$$E = E_{\text{Total}} K = P\pi(R + r)^2 SK \tag{6}$$

In this experiment, the surface with SMGT treatment showed a morphology with plenty of micropits inside the pit and overlaps between pits. According to Figure 13a, it can be seen that, in the process of the three-phase mixed abrasive impact on the surface layer, the steel beads mainly provide the impact kinetic energy for the processed surface to obtain plastic deformation energy. Then plastic deformation occurs, and pits are produced.

Moreover, steel beads also transfer part of the kinetic energy to the abrasive powder attached to its surface. The abrasive powder mainly provides micro-cutting. The abrasive powder with specific kinetic energy is equivalent to the micro-cutting edge, which micro-cuts the inner surface of the pit, thus causing the formation of micropits inside the pit. According to Figure 13b, it can be seen that, as steel beads with strengthened grinding fluids and abrasive powder attached to the surface strike the processed surface to create a pit, the material at the edge of the pit migrates and is extruded, forming a bulge. As the abrasive continuously impacts the process surface, the morphology produced by the previous impact is constantly reshaped, creating the microstructure in that the pit contains micropits and overlaps between the pits.

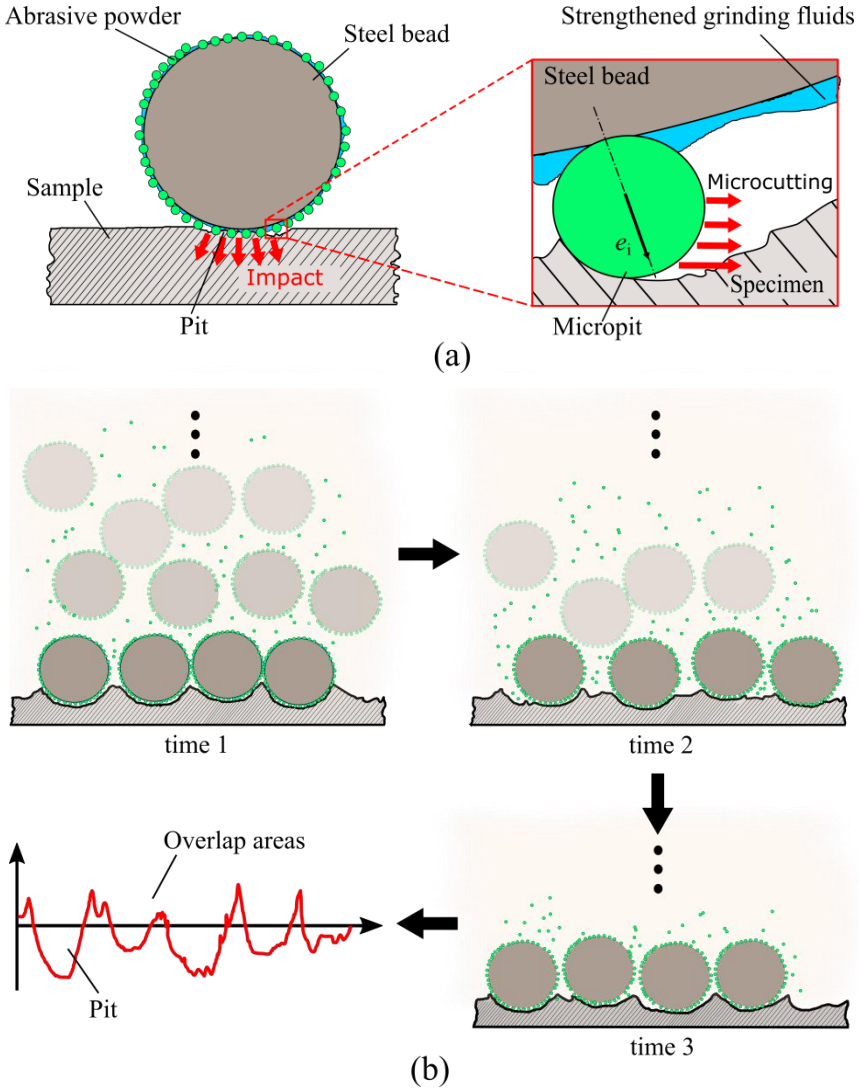

Figure 13. (**a**) Schematic view of impact and micro-cutting; (**b**) Schematic view of the two-dimensional profile.

Related research shows that the energy conversion rate increases with jet velocity. In contrast, when the initial kinetic energy is constant, it mainly depends on the mechanical properties of materials [35]. It is found that the pit width, depth, and bulge height are positively correlated with the jet pressure in this paper. Combining Formulas (4) and (5) and Figure 14a, it is shown that the energy conversion rate is positively correlated with the jet pressure, i.e., $K \propto P$. At a constant jet angle of 90°, the plastic deformation energy in the processed surface is positively correlated with the jet pressure when combined with Formula (6). The increased plastic deformation energy is reflected in the pit width increase

from 123 μm to 221 μm, the pit depth increase from 1.57 μm to 3.52 μm, and the increase in bulge height from 0.62 μm to 1.73 μm. In this paper, the pit width, depth, and bulge height positively correlate with the jet angle. Since the initial total kinetic energy remains invariant at a constant jet pressure, the energy conversion rate remains invariant. Figure 14b shows that the plastic deformation energy can be decomposed into component E_x in the direction of the processed surface and component E_y in the vertical:

$$E_x = Ecos\theta = P\pi(R+r)^2 SKcos\theta \quad (7)$$

$$E_y = Esin\theta = P\pi(R+r)^2 SKsin\theta \quad (8)$$

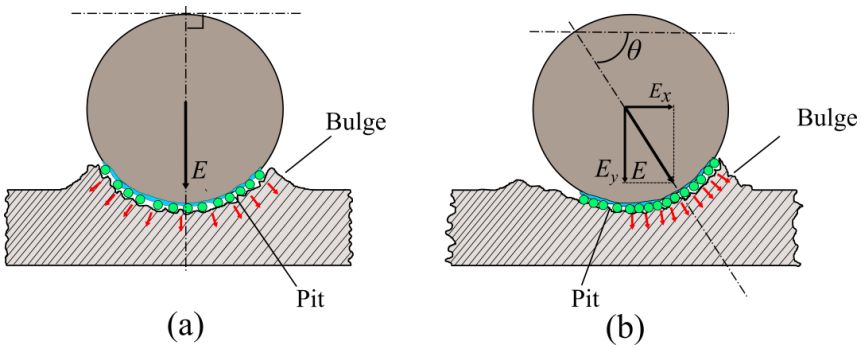

Figure 14. (**a**) Schematic view of the effect of jet pressure on pits; (**b**) Schematic view of the effect of jet angle on pits.

Under the influence of E_y, steel beads deliver an impact force that creates pits on the processed surface. Meanwhile, in the presence of E_x, steel beads are scratched in the direction of the machined surface, with the effect of broadening the already made pits further. As a result, as the jet angle increases, the kinetic energy along the processed surface decreases, and the broadening effect of the pit diminishes, further resulting in the pit width being reduced. While the kinetic energy in the vertical direction increases, the corresponding plastic deformation energy absorbed by the surface layer in the vertical direction also rises.

The hardness of the processed surface is a direct reflection of the wear resistance of the sample. As the jet pressure increased from 0.2 MPa to 0.6 MPa, the hardness increased from 310 $HV_{0.2}$ to 377.6 $HV_{0.2}$. The hardness rose from 310 $HV_{0.2}$ to 362.4 $HV_{0.2}$ and then to 377.6 $HV_{0.2}$ when the jet angle increased from 30° to 60° and then to 90°. By analyzing the morphology of the processed surface with different jet pressures and angles, it is found that the extent of the grain refinement is positively correlated with the jet pressure and angle. On the one hand, plastic deformation of the surface layer caused grain refinement, and the extent of plastic deformation is positively correlated with jet pressure. Accordingly, the extent of grain refinement is positively correlated with the jet pressure. As for the jet angle, the component of plastic deformation energy in the vertical direction is positively correlated with the jet angle. Accordingly, the extent of grain refinement is also positively correlated with the jet angle. On the other hand, the martensite content in the processed surface of the treated samples was increased. The lattice distortions in the processed surface due to plastic deformation induces retained austenite transformation into martensite, and the martensite content becomes positively correlated with the lattice distortion. The strength-modified grinding technique induces grain refinement in the processed surface of 30CrMnSiA bearing steels and causes retained austenite to transform into martensite by producing lattice distortion, which is the main reason for the rise in the surface hardness of the samples.

A summary of the test results for different jet pressures and angles is shown in Table 4.

Table 4. Summary of test results at different jet pressures and angles.

	T0	T1	T2	T3	T4	T5
Jet Pressure (MPa)	None	0.2	0.4	0.6	0.6	0.6
Jet angle (°)	None	90	90	90	60	30
Pit width (μm)	None	123	166	221	248	273
Pit height (μm)	None	1.57	2.64	3.52	1.71	1.18
Bulge height (μm)	None	0.62	1.41	1.73	0.64	0.48
Average grain size (μm)	17.40	14.11	12.62	10.14	13.35	15.61
Martensite content (%)	44.16	45.93	47.62	51.35	49.04	46.27
Surface hardness ($HV_{0.2}$)	310	344.2	356.8	377.6	362.4	350.1

5. Conclusions

(1) In the treatment process of the strength-modified grinding technique (SMGT), the steel beads provide the kinetic energy of impact, and the processed surface undergoes plastic deformation to create a pit. Meanwhile, the abrasive powder attached to the surface of steel beads gains some kinetic energy to micro-cut the inside of the created pit, resulting in a surface microstructure with plenty of micropits inside the pit.

(2) Under the experimental conditions in this paper, the pit width, depth, and bulge height tend to increase as the jet pressure increases, as the extent of plastic deformation is positively correlated with the jet pressure. Since the extent of plastic deformation is positively correlated with the component of plastic deformation energy in the vertical direction, and the component of plastic deformation energy in the direction of the processed surface has a broadening effect on the pit, the pit depth and bulge height show an increasing trend as the jet angle increases, while the pit width shows a decreasing trend.

(3) The SMGT treatment has a strengthening effect on the processed surface of 30CrMnSiA steel. When a pit micromorphology is produced, plenty of plastic deformation leads to grain refinement, and the lattice distortion induces retained austenite to transform into martensite. Grain size decreases with increasing jet pressure and jet angle, and martensite content positively correlates with jet pressure and jet angle.

(4) Under the combined effects of the grain refinement and increased martensite content, the microhardness on the processed surface with SMGT treatment is more potent than in the control group (310 $HV_{0.2}$). The microhardness of the processed surface increases with jet pressure and jet angle, and it is negatively correlated with grain size and positively correlated with martensite content. Group T3 had the highest surface hardness at 377.6 $HV_{0.2}$, an increase of 21.81% compared to the control group.

Author Contributions: Conceptualization, X.L., X.C., Z.L. (Zhongwei Liang), T.Z. and Z.L. (Zhaoyang Liu); methodology, X.L., X.C. and Z.L. (Zhongwei Liang); formal analysis, X.C. and Z.L. (Zhaoyang Liu); investigation, X.C. and B.H.; resources, X.L. and Z.L. (Zhongwei Liang); data curation, X.C. and B.H.; writing—original draft preparation, X.C.; writing—review and editing, X.C. and Z.L. (Zhaoyang Liu); supervision, X.L., Z.L. (Zhaoyang Liu) and Z.L. (Zhongwei Liang); project administration, X.L. and Z.L. (Zhongwei Liang); funding acquisition, X.L. and Z.L. (Zhongwei Liang). All authors have read and agreed to the published version of the manuscript.

Funding: The National Natural Science Foundation of China (51975136, 52075109), National Key Research and Development Program of China (2018YFB2000501), the Science and Technology Innovative Research Team Program in Higher Educational Universities of Guangdong Province (2017KCXTD025), Special Research Projects in the Key Fields of Guangdong Higher Educational Universities (2019KZDZX1009), the Science and Technology Research Project of Guangdong Province (2017A010102014), the Industry–University–Research Cooperation Key Project of Guangzhou Higher Educational Universities (202235139), and Guangzhou University Research Project (YJ2021002).

Institutional Review Board Statement: Not applicable.

Informed Consent Statement: Not applicable.

Data Availability Statement: Not applicable.

Conflicts of Interest: The authors declare no conflict of interest.

References

1. Lei, Z.; Li, B.; Ni, L.; Yang, Y.; Yang, S.; Hu, P. Mechanism of the crack formation and suppression in laser-MAG hybrid welded 30CrMnSiA joints. *J. Mater. Process. Technol.* **2017**, *239*, 187–194. [CrossRef]
2. Wang, T.; Yu, B.; Wang, Y.; Jiang, S. Effect of beam current on microstructures and mechanical properties of joints of TZM/30CrMnSiA by electron beam welding. *Chin. J. Aeronaut.* **2021**, *34*, 122–130. [CrossRef]
3. Feng, Z.; Zhao, H.; Tan, C.; Zhu, B.; Xia, F.; Wang, Q.; Chen, B.; Song, X. Effect of laser texturing on the surface characteristics and bonding property of 30CrMnSiA steel adhesive joints. *J. Manuf. Processes* **2019**, *47*, 219–228. [CrossRef]
4. Wang, S.; Chen, S.; Li, X.; Wan, L. Microstructures and Mechanical Properties of 30CrMnSiA Steel Joints Welded by Vacuum Electron Beam. In Proceedings of the Robotic Welding, Intelligence and Automation, Shanghai, China, 25–27 October 2014; pp. 571–580. [CrossRef]
5. Li, N.; Zhang, W.; Xu, H.; Cai, Y.; Yan, X. Corrosion Behavior and Mechanical Properties of 30CrMnSiA High-Strength Steel under an Indoor Accelerated Harsh Marine Atmospheric Environment. *Materials* **2022**, *15*, 629. [CrossRef]
6. Li, F.; Zhao, S.; Zhu, C.; Zhang, P.; Jiang, H. Influence of process parameters on the forming results of large-sized cylindrical parts during counter-roller spinning. *J. Adv. Mech. Des. Syst. Manuf.* **2022**, *16*, JAMDSM0009. [CrossRef]
7. Qu, S.; Lai, F.; Wang, G.; Yuan, Z.; Li, X.; Guo, H. Friction and Wear Behavior of 30CrMnSiA Steel at Elevated Temperatures. *J. Mater. Eng. Perform.* **2016**, *25*, 1407–1415. [CrossRef]
8. Liu, T.; Qi, X.; Shi, X.; Zhang, T.; Zhang, G.; Zhang, J. Crack growth path of 30CrMnSiA steel under variable amplitude multiaxial loading. *Int. J. Fatigue* **2021**, *153*, 106502. [CrossRef]
9. Tan, Z.H.; Guo, Q.; Li, X.; Zhao, Z.P. The Tribological Behaviour of Beryllium Copper Alloy QBe2 against 30CrMnSiA Steel under Sliding Condition. In Proceedings of the Advanced Materials Research, Beihai, China, 23–25 December 2011; pp. 2181–2188. [CrossRef]
10. Liu, T.; Qi, X.; Shi, X.; Gao, L.; Zhang, T.; Zhang, J. Effect of Loading Frequency Ratio on Multiaxial Asynchronous Fatigue Failure of 30CrMnSiA Steel. *Materials* **2021**, *14*, 3968. [CrossRef]
11. Zhou, J.S.; Zhen, L.; Yang, D.Z.; Li, H.T. Macro- and microdamage behaviors of the 30CrMnSiA steel impacted by hypervelocity projectiles. *Mater. Sci. Eng. A* **2000**, *282*, 177–182. [CrossRef]
12. Fu, Y.; Hu, J.; Shen, X.; Wang, Y.; Zhao, W. Surface hardening of 30CrMnSiA steel using continuous electron beam. *Nucl. Instrum. Methods Phys. Res. Sect. B Beam Interact. Mater. At.* **2017**, *410*, 207–214. [CrossRef]
13. Tang, L.; Yan, M. Microstructure and mechanical properties of surface layers of 30CrMnSiA steel plasma nitrocarburized with rare earth addition. *J. Rare Earths* **2012**, *30*, 1281–1286. [CrossRef]
14. Yan, M.; Wang, Y.; Chen, X.; Guo, L.; Zhang, C.; You, Y.; Bai, B.; Chen, L.; Long, Z.; Li, R. Laser quenching of plasma nitrided 30CrMnSiA steel. *Mater. Des.* **2014**, *58*, 154–160. [CrossRef]
15. Xiao, J.; Liu, X.; Xie, B.; Liu, C.; Zhang, J.; He, Q. Study on the optimal velocity of reinforced grinding of bearing ring raceway. *Hydromechatronics Eng.* **2014**, *42*, 56–61+106. [CrossRef]
16. Liu, X.; Wen, Y.; Liang, Z.; Liao, S.; Ji, W. Effect of Bearing Steel Balls Diameter Ratio for Surface Hardness and Morphology of Bearing Ring in Reinforced Grinding Processing. *Mach. Tool Hydraul.* **2017**, *45*, 123–126. [CrossRef]
17. Liu, X.; Chen, F.; Zhang, C.; Shan, S.; Liao, S. Experiment and Research of Abrasive Ratio Based on Reinforced Grinding Processing. *Tool Eng.* **2016**, *50*, 27–30. [CrossRef]
18. Liu, X.; Zhao, C.; Li, F.; Qin, Z.; Zhou, W.; Chen, F. Analysis of Residual Stress in Bearing Rings of Reinforced Grinding. *Modul. Mach. Tool Autom. Manuf. Tech.* **2017**, *4*, 5–8. [CrossRef]
19. Liu, X.; Qin, Z.; Xiao, J.; Zhao, C.; Chen, Y. Evaluation for Wear Failure of Strengthening Abrasive Based on Image Processing. *Bearing* **2018**, *11*, 26–29+60. [CrossRef]
20. Xiao, J.; Zhao, Z.; Xie, X.; Liang, Z.; Liu, Z.; Liu, X.; Tang, R. Micromorphology, Microstructure, and Wear Behavior of AISI 1045 Steels Irregular Texture Fabricated by Ultrasonic Strengthening Grinding Process. *Metals* **2022**, *12*, 1027. [CrossRef]
21. Xie, X.; Guo, Z.; Zhao, Z.; Liang, Z.; Wu, J.; Liu, X.; Xiao, J. Salt-Fog Corrosion Behavior of GCr15 Steels Treated by Ultrasonic Strengthening Grinding Process. *Appl. Sci.* **2022**, *12*, 7360. [CrossRef]
22. Liu, X.; Wu, Z.; Liang, Z.; Wu, J.; Fan, L.; Geng, C.; Xie, X.; Huang, W.; Wei, S. Effect of Spray Angle on Friction and Corrosion Resistance of GCr15 Bearing Steel in Strengthening Grinding. *Mech. Electr. Eng. Technol.* **2021**, *50*, 1–5. [CrossRef]
23. Xiao, J.; Liu, X.; Liang, Z.; Xiao, Z. Effect of Steel Bead's Damage on the Surface Roughness and Hardness of Bearing Rings under Strengthen Grinding Processing. *Surf. Technol.* **2018**, *47*, 290–295. [CrossRef]
24. Xiao, J.; Liang, Z.; Huang, J.; Gao, W.; Liu, X.; Chen, Y. Effect of Strengthen Grinding on the Surface Corrosion Resistance of Bearing Ring. *Surf. Technol.* **2021**, *50*, 238–244+294. [CrossRef]
25. Liu, X.; Huang, J.; Liang, Z.; Huang, W.; Zhu, R.; Gao, W.; Xiao, J. Preparation and Properties of the Composite Enhancement Layer of Bearing Ring. *World J. Mech.* **2020**, *10*, 139–153. [CrossRef]
26. Liu, X.; Geng, C.; Ruan, Y.; Liang, Z.; Feng, W.; Fan, L.; Wu, Z.; Wu, J. Effect of Strengthened Grinding Jet Pressure on Stress Corrosion Properties of GCr15 Bearing Steel. *Mech. Electr. Eng. Technol.* **2022**, *51*, 6–9+85.
27. Farhat, Z.N.; Ding, Y.; Northwood, D.O.; Alpas, A.T. Effect of grain size on friction and wear of nanocrystalline aluminum. *Mater. Sci. Eng. A* **1996**, *206*, 302–313. [CrossRef]

28. Zhang, H.; Dong, X.; Wang, Q.; Li, H. Micro-bending of metallic crystalline foils by non-local dislocation density based crystal plasticity finite element model. *Trans. Nonferrous Met. Soc. China* **2013**, *23*, 3362–3371. [CrossRef]
29. Khun, N.W.; Trung, P.Q.; Butler, D.L. Mechanical and Tribological Properties of Shot-Peened SAE 1070 Steel. *Tribol. Trans.* **2016**, *59*, 932–943. [CrossRef]
30. Nespolo, M.; Souvignier, B. Application of the crystallographic orbit analysis to the study of twinned crystals. The example of marcasite. *Cryst. Res. Technol.* **2015**, *50*, 442–450. [CrossRef]
31. Wang, F.; Hazeli, K.; Molodov, K.D.; Barrett, C.D.; Al-Samman, T.; Molodov, D.A.; Kontsos, A.; Ramesh, K.T.; El Kadiri, H.; Agnew, S.R. Characteristic dislocation substructure in {10(1)over-bar2} twins in hexagonal metals. *Scr. Mater.* **2018**, *143*, 81–85. [CrossRef]
32. Niho, T.; Nambu, S.; Nagato, K.; Nakao, M. Classification of Twin Arrangements in Butterfly Martensite Grains and Analysis of Relationship between Twin Arrangement and Butterfly Wing Angle in Medium-Carbon Steel. *ISIJ Int.* **2020**, *60*, 2075–2082. [CrossRef]
33. Ma, B.; Fu, L.; ShangGuang, B.; Du, S.; Mao, Y.; Yue, Y.; Zhang, Y. Friction and wear Properties of Gcr15 and G20CrNi2Mo Bearing Steels under High Temperture Lubrication. *Lubriction Eng.* **2022**, *47*, 62–68. [CrossRef]
34. Xiong, X.; Chen, J.; Yao, P.; Li, S.; Huang, B. Friction and wear behaviors and mechanisms of Fe and SiO_2 in Cu-based P/M friction materials. *Wear* **2007**, *262*, 1182–1186. [CrossRef]
35. Yan, W.; Liu, J.; Wen, S.; Yue, Z. Energy conversion and residual stress distribution in shot peening process. *J. Vib. Shock* **2011**, *30*, 139–142+191. [CrossRef]